Studies on thermal-hydraulic characteristics of supercritical CO_2 flows with non-uniform heat flux in a tubular solar receiver

Xiaokai Liu[a,b], Jiangfeng Guo[a,b,c,d,*], Zengxiao Han[a,b], Keyong Cheng[a,b,d], Xiulan Huai[a,b,d]

[a]*Institute of Engineering Thermophysics, Chinese Academy of Sciences, Beijing 100190, China*

[b]*School of Engineering Science, University of Chinese Academy of Sciences, Beijing 100049, China*

[c]*Clean Energy Processes (CEP) Laboratory, Department of Chemical Engineering, Imperial College London, London SW7 2AZ, UK*

[d]*Nanjing Institute of Future Energy System, Nanjing 211135, China*

Abstract

Supercritical CO_2 (SCO_2) Brayton cycle is one of the best approaches for concentrated solar power tower, with tubular solar receiver being one of the most attractive options to directly heat SCO_2. The superposition of drastically variable properties of SCO_2 and uneven distribution of solar irradiance flux poses a great challenge to the design and optimisation of solar receiver, thus the studies on thermal-hydraulic characteristics of SCO_2 in solar receiver become crucial to deal with the challenge. In this study, the thermal-hydraulic characteristics of SCO_2 in a vertical receiver tube under axially and circumferentially non-uniform heat-flux conditions are numerically studied with average heat flux ranging from 150 $kW{\cdot}m^{-2}$ to 210 $kW{\cdot}m^{-2}$ and mass flux ranging from 400 $kg{\cdot}m^{-2}{\cdot}s^{-1}$ to 700 $kg{\cdot}m^{-2}{\cdot}s^{-1}$, and the influences of buoyancy on the flow and heat transfer characteristics are evaluated. The non-uniform distribution of the axial heat flux leads to 1.2% to 20.5% increase in the overall heat transfer coefficient, while more serious local heat transfer deterioration is observed. The buoyancy effect changes the flow structure, resulting in suppression of turbulence intensity and formation of thick momentum and thermal boundary layers, which is closely related to the severe heat transfer deterioration of SCO_2 under non-uniform heat-flux conditions. Bo^* could well predict the buoyancy effect in a vertical tube under non-uniform heat-flux conditions. Compared with upward flow, downward flow could effectively alleviate heat transfer deterioration and reduce wall temperature gradient especially for axially non-uniform heat-flux condition. The present work could provide guideline for the design and optimisation of tubular solar receiver and solar power system with SCO_2 as heat transfer fluid.

Key words: Supercritical CO_2 (SCO_2); non-uniform heat-flux condition; solar tower power; thermal-hydraulic characteristics; solar receiver.

*Corresponding author. *E-mail address*: guojf@iet.cn, gjf1200@126.com (J. Guo).

Nomenclature

a	acceleration, $m \cdot s^{-2}$
Bo^*	non-dimensional buoyancy parameter,
c_p	specific heat at constant pressure, $kJ \cdot kg^{-1} \cdot K^{-1}$
D	diameter, mm
g	gravity, $m \cdot s^{-2}$
G	mass flux, $kg \cdot m^{-2} \cdot s^{-1}$
Gr^*	Grashof number
h	heat transfer coefficient, $kW \cdot m^{-2} \cdot K^{-1}$
H	enthalpy $kJ \cdot kg^{-1}$
k	turbulence kinetic energy, $m^2 \cdot s^{-2}$
L	heated length or distance from the position where heating starts, m
P	Pressure, MPa
P_k	production of turbulence energy, $kg \cdot m^{-1} \cdot s^{-3}$
Pr	Prandtl number
q	heat flux, $kW \cdot m^{-2}$
r	radial coordinate, mm
R	tube radius, mm
Re	inlet Reynolds number
T	temperature, K
T_{pc}	pseudocritical temperature, K
v	velocity, $m \cdot s^{-1}$
x, y, z	x, y, z directions
y^+	non-dimensional distance from the wall

Greek symbols

β	volume expansion coefficient, K^{-1}
θ	circumferential angle, degree
λ	thermal conductivity, $W \cdot m^{-1} \cdot K^{-1}$

μ	dynamic viscosity, Pa·s
μ_t	turbulent viscosity, Pa·s
ν	kinematic viscosity, $m^2 \cdot s^{-1}$
ρ	density, $kg \cdot m^{-3}$
σ	standard deviation of the Gaussian distribution
τ	shear stress, Pa
ϕ	energy dissipation, $W \cdot m^{-3}$
Subscripts	
ave	average
b	bulk
c	critical
i, j, l	tensor index symbols
in	inlet section
m	median
max	maximum
min	minimum
w	wall

1. Introduction

With the increasingly serious climate problems, reducing carbon emissions, achieving carbon neutrality and controlling global warming have become the consensus in today's world. In order to achieve sustainable development goals (SDGs) and Net zero targets, it is of great significance to develop highly efficient, environmentally friendly energy conversion technologies. The power cycle using CO_2 as a working medium has received extensive attention in recent decades. The supercritical CO_2 (SCO_2) Brayton cycle system can significantly reduce compressor power consumption and system size, improve system efficiency, decrease investment costs, and simplify system design [1,2]. This system has promising potentials in concentrating solar systems [3], geothermal energy [4], fourth-generation nuclear power systems [5], new gas turbines and coal-fired power plants [6,7], etc. Heat exchanger is a key component in SCO_2 Brayton cycle system which has a significant impact on the performance and cost of the entire system. However, unlike conventional fluids,

SCO_2 drastically changes in thermophysical properties near the critical or pseudocritical point, which makes flow and heat transfer of SCO_2 unique and interesting.

Experiment studies on SCO_2 have been conducted to investigate the effects of mass flux, heat flux, pipe diameter and other operating parameters on the flow and heat transfer characteristics (also known as thermal-hydraulic characteristics) of SCO_2 in the past several decades [8,9]. Kim et al. [10,11] experimentally studied the heat transfer of SCO_2 in upward and downward flows in a tube with diameter of 4.5 mm, and they found at the conditions of G = 489 $kg \cdot m^{-2} \cdot s^{-1}$ and q = 85 $kW \cdot m^{-2}$ (medium wall heat flux and low mass flux), an obvious peak was observed for the wall temperature in upward flow while this peak did not appear in downward flow. Lei et al. [12] experimentally investigated the heat transfer characteristics of SCO_2 in a vertical small channel with mass flux ranging from 50 to 200 $kg \cdot m^{-2} \cdot s^{-1}$ and heat flux ranging from 38 to 234 $kW \cdot m^{-2}$. They reported that significant difference was observed in heat transfer characteristics at different heat-flux levels in small tubes. Heat transfer of SCO_2 may deteriorate in vertical heating tubes, a criterion combined with Grashof number was proposed by Jackson et al. [13] to determine the occurrence of heat transfer deterioration. Kline et al. [14] stated that the minimum heat flux that triggered heat transfer deterioration followed the power law of mass flux in vertical tubes. In addition, Ershan et al. [15] and Xie et al. [16] reviewed the empirical correlations for heat transfer of SCO_2 in horizontal and vertical tubes under heating and cooling conditions, but no one could predict the heat transfer performance accurately under various working conditions.

Due to the difficulty of obtaining detailed information about the internal heat transfer and flow features through experiment, numerical methods have also been widely used to explore the complex heat transfer mechanism of supercritical fluids. Xiang et al. [17] and Li et al. [18] found that heat transfer deterioration was observed at the bottom region of horizontal cooled flows, while heat transfer deterioration occurred in the top region under horizontal heating conditions. Wang et al. [19] studied the buoyancy effect of SCO_2 in large horizontal tubes, and they concluded that buoyancy influenced the flow structure and turbulence levels mainly via the induced secondary flow. Guo et al. [20] used the variable turbulence Prandtl number model to study the flow and heat transfer characteristics of SCO_2 in a vertical tube, with results showing that the local heat transfer deterioration of SCO_2 was alleviated by reducing the heat flux density and pipe diameter. Zhao et al. [21] compared the heat transfer behaviour and mechanism of SCO_2 for upward and downward flows, and they found that the buoyancy effect influenced the viscous length scale and the redistribution of the velocity profiles. Some enhanced tubes such as helically coiled tubes [22] and cylindrically concaved tubes [23] were also employed to eliminate localized heat transfer deterioration and effectively improve heat transfer performance under uniform heating conditions.

The researches on the thermal-hydraulic characteristics of SCO_2 were generally conducted under uniformly heating or cooling conditions in existing literature. However, in practical applications such as coal-fired power generation system and solar thermal power system, the heat flux distribution on the surface of the heat absorber exhibits extremely nonuniform. The schematic diagram of the structure of the solar power tower and the solar irradiance flux on the receiver focal plane are presented in Figure 1 [24]. The solar heat collection system in solar power tower is mainly composed of solar heliostat field, tower and solar receiver [25]. From the solar irradiance flux on the focal plane as shown in Figure 1(b), it is obvious that the solar flux on the surface of the receiver is non-uniformly distributed in both the axial and circumferential directions, and this brings severe challenges to the design of receiver in SCO_2 power system.

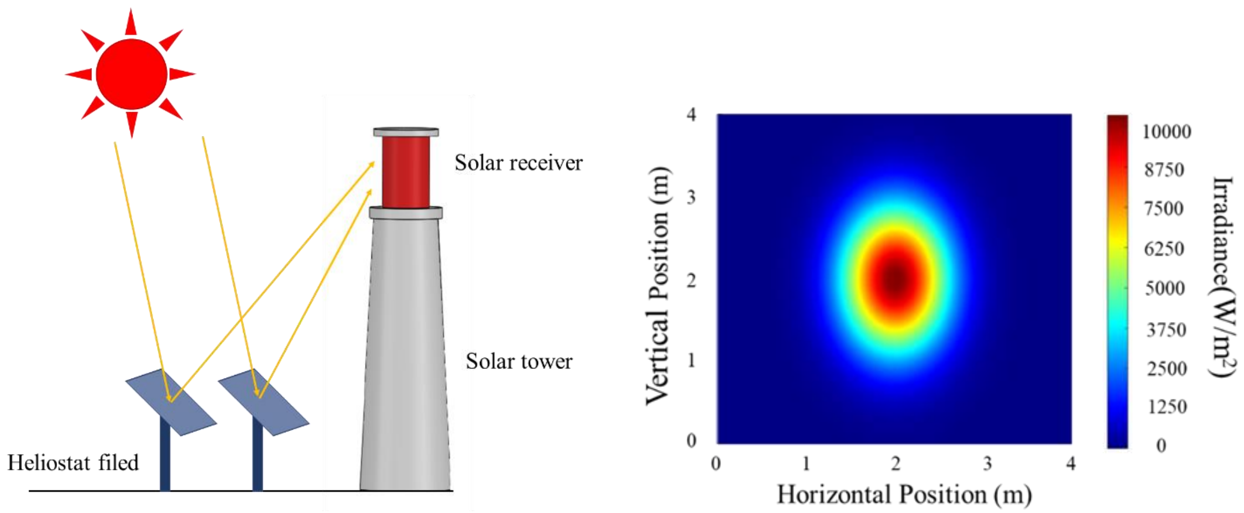

(a) solar power tower (b) measured heat flux

Figure 1. Schematic diagrams of (a) solar power tower and (b) heat flux on the receiver focal plane [24].

The design and optimization for future SCO_2 solar power tower requires a comprehensive and in-depth understanding of the heat transfer and flow characteristics of SCO_2 with various heat-flux distributions. The heat transfer behaviours of supercritical fluids are complex due to the drastically variable thermophysical properties near the pseudocritical temperature (T_{pc}). Although the near-pseudocritical region of CO_2 is not the main heating condition in the Brayton power cycle, the dynamic oscillation of the operating conditions during transitions such as from start-up to full-load [26] may lead to CO_2 near the pseudocritical region in the solar receiver [27,28]. Therefore, it is necessary to study thermal-hydraulic characteristics of SCO_2 near the pseudocritical region in vertical tubes with axially and circumferentially non-uniform heat-flux distribution.

The non-uniform heat-flux distribution would lead to a great difference to the heat transfer performance of SCO_2 in tubular solar receiver [29]. However, the reports on the thermal-hydraulic characteristics of SCO_2 under non-uniform heat-flux conditions are very few in existing literature, especially for vertical flows under circumferentially and axially non-uniform heat-flux conditions.

To bridge the gap between the existing researches and the practical applications in solar energy, the thermal-hydraulic characteristics of SCO_2 in a vertical tubular solar receiver under axially and circumferentially non-uniform heat-flux distributions for a solar power tower system are numerically studied in the present work, the effects of heat flux, mass flux and flow directions on the thermal-hydraulic characteristics of SCO_2 under four types of non-uniform heating conditions are investigated and analysed, and the buoyancy effect under the various heat-flux distributions is discussed in detail as well. The conclusions of this work provide insight of thermohydraulic characteristics of supercritical CO_2 flows as well as useful guidance for design and optimisation of tubular solar receiver and solar power system using supercritical CO_2 as heat transfer fluid.

2. Numerical methodology

2.1. Physical model and boundary conditions

The influence of the solid domain on the heat transfer is considered under the non-uniform heating condition in this study. The 316L stainless steel is selected as the material of the tube. The inner diameter of the tube is 6 mm and the wall thickness is set as 1 mm. We mainly focus on the flow and heat transfer characteristics of SCO_2 in the near-pseudocritical region under non-uniform heat-flux conditions, so the length of the heated section is 1,200 mm as shown in Figure 2, which is enough to conduct the studies within the ranges considered in the present work. The adiabatic sections of 300 mm and 200 mm are adopted in entrance and exit regions to eliminate the effect of unstable flow.

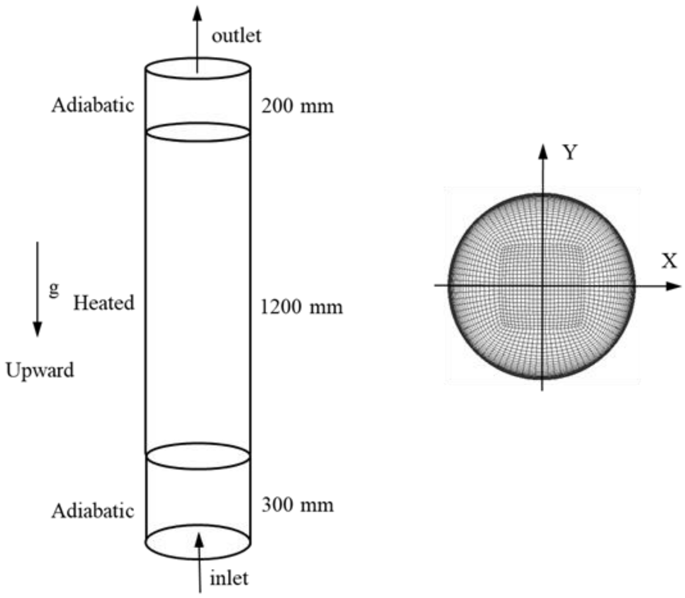

Figure 2. Physical model considered in the present work, with inner diameter of 6 mm, wall thickness of 1 mm, non-adiabatic length of 1,200 mm, and adiabatic length of 300 mm and 200 mm in the entrance and exit regions, respectively.

The heat-flux distribution on the solar thermal collector is complex in the solar power tower system, only one side of receiver wall is exposed to solar radiation. The HFLCAL (short for Heliostat Field Layout CALculation) model [32] is one of the most widely used analytical models with a simple and closed-form expression to calculate the heat-flux distribution of the heat receiver in solar power tower system [33]. This model based on the Gaussian distribution is adopted in the present work. We only focus on the heat transfer characteristics of SCO_2 in a single receiver tube, the heat-flux distribution on receiver wall is supposed to follow the Gaussian distribution along the axial direction and cosine distribution on the semi-circumference side [34,35]. The heat-flux distribution is calculated as follows [36]:

$$q = \frac{q_{\max}}{\sqrt{2\pi}\sigma} \exp\left(-\frac{(z - z_m)^2}{2\sigma^2}\right) \tag{1}$$

$$q = q_{ave} \cdot \pi \cdot \cos\theta \tag{2}$$

where σ is the standard deviation of the Gaussian distribution, $q_{\max}$ and q_{ave} represent the maximum and average heat flux of the Gaussian distribution, z represents the coordinate on axial direction, z_{m} is the median of z.

According to the heat-flux distribution of solar power tower experimentally measured in Ref. [37], the value of standard deviation of the Gaussian distribution is set as 0.3 when the heating length of the solar receiver tube is 1.2 m in the present work, and the axially heat-flux distribution is shown in Figure 3.

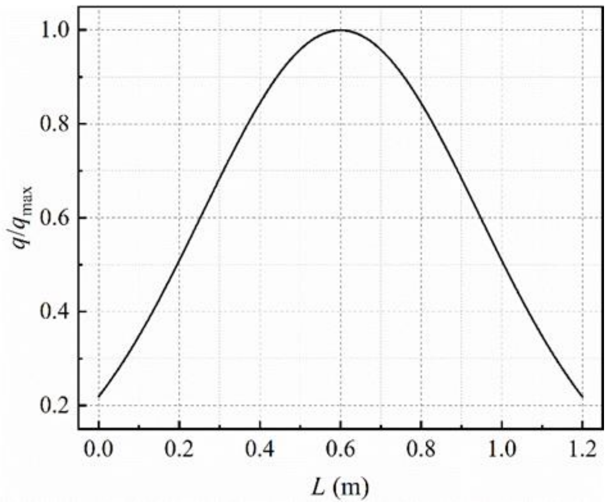

Figure 3. Distribution of the axial heat flux at the condition of axially non-uniform heat flux.

Four types of heat-flux conditions are considered to study the effect of heat-flux distribution on the thermal-hydraulic characteristics of SCO_2, which are presented in Figure 4. They are circumferentially and axially uniform distribution (Case 1), semi-circumferentially and axially uniform distribution (Case 2), semi-circumferentially non-uniform and axially uniform distribution (Case 3), semi-circumferentially and axially non-uniform distribution (Case 4) respectively. In order to locate the position on the transverse sections, the lowest point of the tube in the negative y-direction is set to be 180°, the highest point is set to be 0°, and the leftmost and rightmost point are set to be -90° and 90° respectively. For semi-circumferential cases, the heat flux is only imposed on the wall of $-90° \leq \theta \leq 90°$ (top half of the tube wall shown in Figure 4(b)). To further describe the four heat fluxes quantitatively, the expressions for the four types of heat-flux distributions are listed in Table 1. It should be noted that the total heat transfer rate under four heat-flux conditions is the same when the average heat flux q_{ave} is fixed. The inlet temperature and outlet pressure are fixed as 304 K and 8 MPa ($T_{pc} \approx 307.8$ K at $P = 8$ Mpa) in all Cases. The velocity distribution and Reynolds number at the end of the inlet adiabatic section are carefully checked to ensure that the turbulence is fully developed before being heated in all cases. The Reynolds number ranges from 20,000 to 120,000 in the simulations, which conforms to the operating conditions of solar energy plants [31,38].

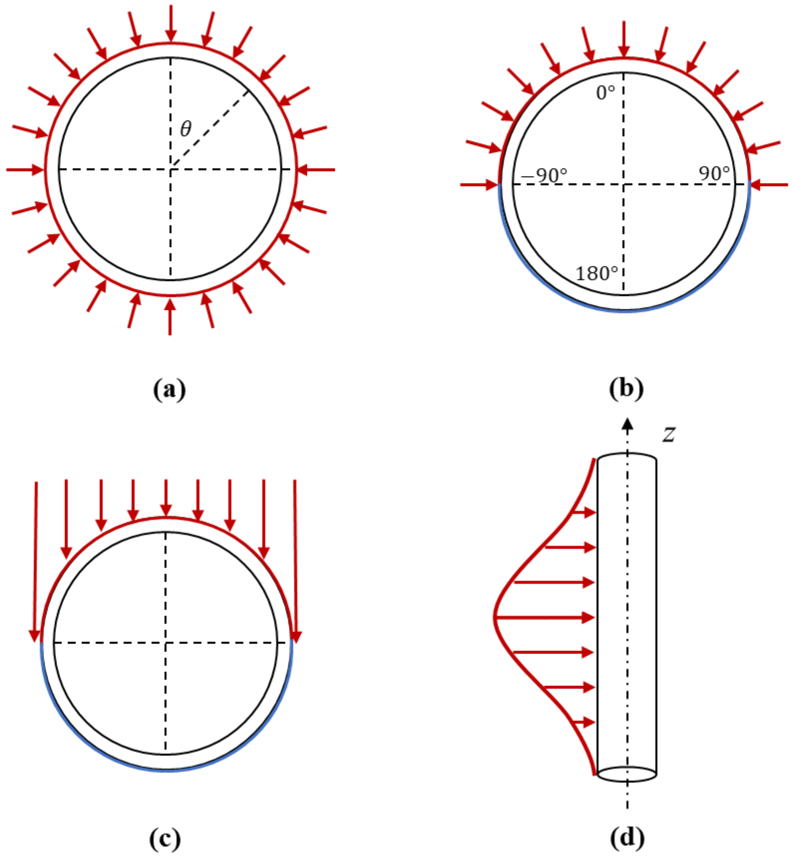

Figure 4. Four types of heat-flux conditions: (a) circumferentially uniform, (b) semi-circumferentially uniform, (c) semi-circumferentially non-uniform, (d) axially non-uniform in the vertical tube. The average equivalent heat flux remains constant in the four types of heat flux conditions.

Table 1. Expressions for the four types of heat-flux conditions with the same total heat transfer rate.

	Heating condition	Heat flux expression/kW·m^{-2}
Case 1	circumferentially uniform axially uniform	$q = q_{ave}$
Case 2	semi-circumferentially uniform axially uniform	$q = 2 \cdot q_{ave}$
Case 3	semi-circumferentially non-uniform axially uniform	$q = q_{ave} \cdot \pi \cdot \cos\theta$
Case 4	semi-circumferentially non-uniform axially non-uniform	$q = 0.76 \cdot q_{ave} \cdot \pi \cdot \exp(-4.233 \cdot (z-0.6)^2) \cdot \cos\theta$

2.2. Governing equations

The numerical calculation is carried out using ANSYS CFX 16.0 in the present work [39]. It's assumed that the heat transfer remains steady state. The heat loss of the receiver in solar tower power plant could be effectively reduced to a very small percentage by adjusting cavity shapes, optimizing the surface radiation properties, etc., which has little effect on the heat-flux distribution on the wall and the thermal-hydraulic characteristics of fluid in the tube. Thus, the heat exchanged with ambient environment is neglected in the present work. The governing equations in solid domain and fluid domain are listed as follows [39].

Continuity equation:

$$\frac{\partial(\rho u_j)}{\partial x_j}=0 \tag{3}$$

Momentum equation:

$$\frac{\partial(\rho u_i u_j)}{\partial x_j}=-\frac{\partial P_i}{\partial x_j}+\rho g_i+\frac{\partial}{\partial x_j}\left[(\mu+\mu_t)(\frac{\partial u_i}{\partial x_j}+\frac{\partial u_i}{\partial x_j}-\frac{2}{3}\frac{\partial u_l}{\partial x_l})\right] \tag{4}$$

Energy equation for fluid domain:

$$\frac{\partial(\rho u_j c_p T)}{\partial x_j}=\frac{\partial}{\partial x_j}(\lambda\frac{\partial T}{\partial x_j})+\phi \tag{5}$$

Energy equation for solid domain:

$$\frac{\partial}{\partial x_j}(\lambda_s\frac{\partial T}{\partial x_j})=0 \tag{6}$$

where ρ is density, μ is dynamic viscosity, μ_t is turbulent viscosity, λ and λ_s represents thermal conductivity of fluid and solid domains. ϕ is the energy dissipation, c_p represents the specific heat at constant pressure, g is gravitational acceleration.

The Shear-Stress Transport (SST) model [40] has advantages in robusticity near the wall and accuracy in the region apart from the wall which could result in relatively accurate simulation especially for supercritical fluids, which has been verified by lots of studies in the existing literature [29,41]. Thus, SST turbulence model is employed in the present work. The transport equations for SST turbulence model are defined as follows [42]:

Turbulence kinetic energy k:

$$\frac{\partial(\rho k)}{\partial t}+\frac{\partial(\rho k u_i)}{\partial x_i}=-\frac{\partial}{\partial x_j}(\Gamma_k\frac{\partial k}{\partial x_j})+G_k-Y_k+S_k \tag{7}$$

Specific dissipation rate ω:

$$\frac{\partial(\rho\omega)}{\partial t}+\frac{\partial(\rho\omega u_i)}{\partial x_i}=-\frac{\partial}{\partial x_j}(\Gamma_\omega\frac{\partial\omega}{\partial x_j})+G_\omega-Y_\omega+S_\omega \tag{8}$$

where G_k represents the production of k, G_ω represents the generation of ω, Γ_k and Γ_ω are the effective diffusivities of k and ω, Y_k and Y_ω represent the dissipation of k and ω respectively. S_k and S_ω are source terms.

A real gas property file containing the thermophysical properties of CO_2 obtained from NIST Standard Reference Database is imported to the ANSYS CFX software [43]. The governing equations are discretized by the finite volume method. High resolution is adopted for calculations in the governing equations. When the residuals for all monitored variables in Eqs. (3) to (8) are less than 1×10^{-6}, the numerical result is considered to be converged.

Numerous slices with equal distance of 50 mm along the flow direction are established to obtain local parameters such as wall temperature and wall heat flux. The overall parameters are obtained from local parameters. The local convective heat transfer coefficient is calculated as follows:

$$h_b = \frac{q_w}{T_w - T_b} \tag{9}$$

where q_w is circumferentially average wall heat flux and T_w is circumferentially average wall temperature. T_b represents the fluid bulk temperature.

The heat transfer coefficient in the circumferential direction may exhibit severe non-uniformity because of the non-uniform heat-flux distribution. The local wall-circumference heat transfer coefficient is defined as follows:

$$h_w(\theta) = \frac{q_w(\theta)}{T_w(\theta) - T_b} \tag{10}$$

where $q_w(\theta)$ and $T_w(\theta)$ are local wall heat flux and wall temperature based on the angular position shown in Figure 4, respectively.

2.3 Grid independence and model validation

To check the grid independence of numerical simulation, four types of grid systems are established by ANSYS ICEM CFD 16.0, and the number of elements is about 3.151×10^6, 3.881×10^6, 4.472×10^6 and 6.329×10^6 respectively. The grid independence test results are shown in Figure 5 by using SST model under the condition of $G = 600$ kg·m^{-2}·s^{-1} and $q_{ave} = 180$ kW·m^{-2}. The maximum relative error of the local heat transfer coefficient between grid 3 and grid 4 is only about 2.6%. Considering the calculation time and accuracy, the grid 3 with 4.472×10^6 elements is employed in the present work.

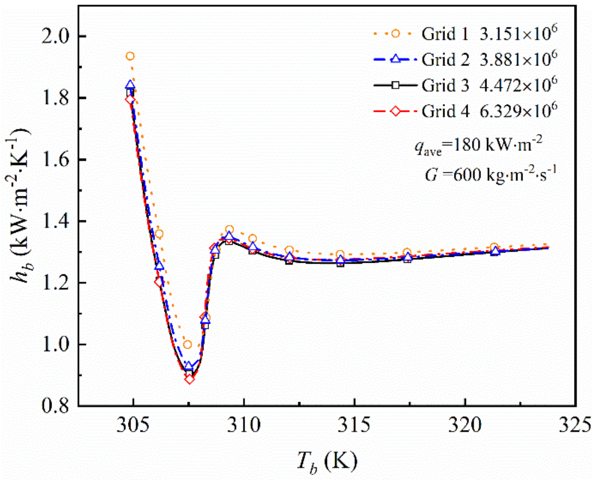

Figure 5. Local heat transfer coefficient distributions with four types of grid systems at the conditions of G = 600 kg·m^{-2}·s^{-1} and q_{ave} = 180 kW·m^{-2}.

Due to the lack of experimental studies on vertical flow of SCO_2 under non-uniform heating condition, the experiment results with uniform heat-flux distribution conducted by Zhang [44] are adopted to validate the accuracy of the model in the present work. A same vertical tube model with diameter of 10 mm is established, and the mass flux of 488 kg·m^{-2}·s^{-1}, inlet temperature of 302.5 K and working pressure of 8.24 MPa in the experiment are adopted to validate the present model. The comparison between the local wall temperature obtained by the simulation and experiment is presented in Figure 6. The maximum relative error of wall temperature between simulation and experiment is about 6.42 %, which could be accepted in the present work. Thus, the numerical model employed in the present work is reliable and acceptable.

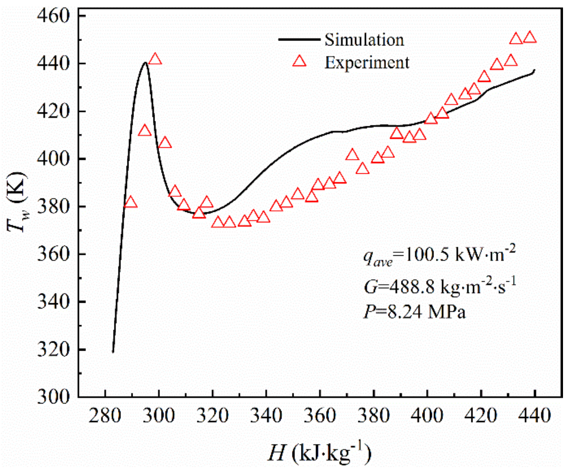

Figure 6. The comparison of wall temperature between the numerical results and experimental results in Ref. [44] at conditions of q_{ave} = 100.5 kW·m^{-2}, G = 488 kg·m^{-2}·s^{-1} and P = 8.24 MPa.

3. Results and discussion

This section is arranged as follows: the flow and heat transfer characteristics of SCO_2 with vertical upward flow under four types of heat-flux conditions listed in Table 1 are studied in section 3.1; in section 3.2, the effects of buoyancy on flow and heat transfer behaviours of SCO_2 are discussed in detail; and finally, the effects of flow directions on heat transfer performance under non-uniform heat-flux conditions are investigated in section 3.3.

3.1. Influence of heat flux and mass flux

In this subsection, the heat transfer performance of SCO_2 in vertical upward flow will be studied under the four types of heat-flux distributions listed in Table 1 based on the model in Figure 1.

The relationship of the overall heat transfer coefficient h with Reynolds number Re under four types of heating conditions listed in Table 1 is presented in Figure 7. The overall heat transfer coefficient increases monotonically with the increase of Re when other conditions are fixed, and the higher the heat flux is, the lower the overall heat transfer coefficient would be. The h of axially non-uniformly heat-flux distribution (Case 4) is 1.2% to 20.5% higher than that of axially uniformly heat-flux distribution (Case 3) under conditions of q_{ave} = 150 to 210 kW·m^{-2} and Re = 4.4 × 10^4 to 7.8 × 10^4, and this discrepancy becomes more significant as the heat flux increases. With the increase of Re, the superiority of axially non-uniformly heating condition becomes more obvious at q_{ave} = 210 kW·m^{-2}. However, this difference of the h between axially non-uniform and axially uniform heating firstly increases and then gradually weakens with the increase of Re at q_{ave} = 150 kW·m^{-2} and q_{ave} = 180 kW·m^{-2}. It can be seen that the h almost coincides together under four types of heating conditions at q_{ave} = 150 kW·m^{-2} and Re = 7.8 × 10^4. When the axially heat flux is uniform, the h of semi-circumferentially non-uniform heating condition (Case 3) is 0.3% to 1.3% higher than that of semi-circumferentially uniform (Case 2) and fully uniform (Case 1) heat-flux conditions. The same phenomenon is also found in the circumferentially non-uniformly vertical heated tube in the numerical study conducted by Fan et al. [27]. Therefore, the overall heat transfer of SCO_2 is enhanced under non-uniform heating conditions.

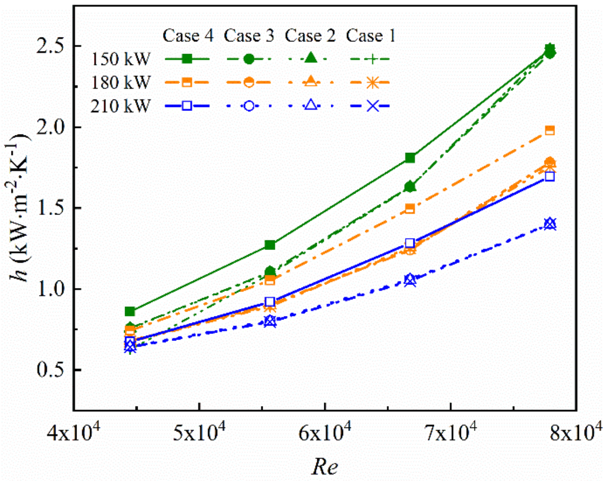

Figure 7. Relationship of overall heat transfer coefficient with inlet *Re* under four types of heat-flux conditions listed in Table 1 at conditions of T_{in} = 304 K, P = 8 MPa, q_{ave} = 150 to 210 kW·m^{-2}.

The relationship of the local bulk heat transfer coefficient h_b with fluid bulk temperature T_b under four types of heat-flux conditions listed in Table 1 with average heat flux ranging from 150 kW·m^{-2} to 210 kW·m^{-2} and mass flux ranging from 500 kg·m^{-2}·s^{-1} to 700 kg·m^{-2}·s^{-1} is shown in Figure 8. Different heat flux distributions lead to significant discrepancies in the local heat transfer behaviour under the same mass-flux and heat-flux conditions. Figure 8(a) depicts the distribution of h_b with various heat fluxes at G = 600 kg·m^{-2}·s^{-1}. It can be seen that there are obvious troughs in h_b under four types of heat-flux conditions at q_{ave} = 180 kW·m^{-2} and q_{ave} = 210 kW·m^{-2}. However, at the condition of q_{ave} = 150 kW·m^{-2}, the trough of the h_b only can be found in Case 4 of axially non-uniform heat-flux distribution and there is no significant trough for axially uniform heating. The distribution of h_b with various mass fluxes under the heat flux of 180 kW·m^{-2} is presented in Figure 8 (b). The h_b have significant troughs along the flow direction in most conditions except in the case of axially uniform heating at G = 700 kg·m^{-2}·s^{-1}. At the same mass flux (G = 500 to 700 kg·m^{-2}·s^{-1}) and average heat flux (q_{ave} = 150 to 210 kW·m^{-2}), the T_b corresponding to the trough of the h_b under the axially non-uniform heating (Case 4) is 1.6 K to 3.3 K higher than that under the axially uniform heat-flux condition (Case 3), and this disparity is more significant at the low heat flux (q_{ave} = 150 kW·m^{-2}) and high mass flux (G = 700 kg·m^{-2}·s^{-1}). It is obvious that the minimum h_b is smaller under the axially non-uniform heat-flux distribution of Case 4 than under other cases. However, the h_b of Case 4 is much higher than that of other heating conditions in the initial heating section of the tube, which is the main reason why the overall h of Case 4 is higher than that of axially uniform heat-flux condition. Based on the above analysis, the overall and local heat transfer coefficients exhibit complex variations under different heating conditions, the local heat transfer characteristics of SCO_2

in a vertical tube are closely related to the mass flux and the local heat flux distribution.

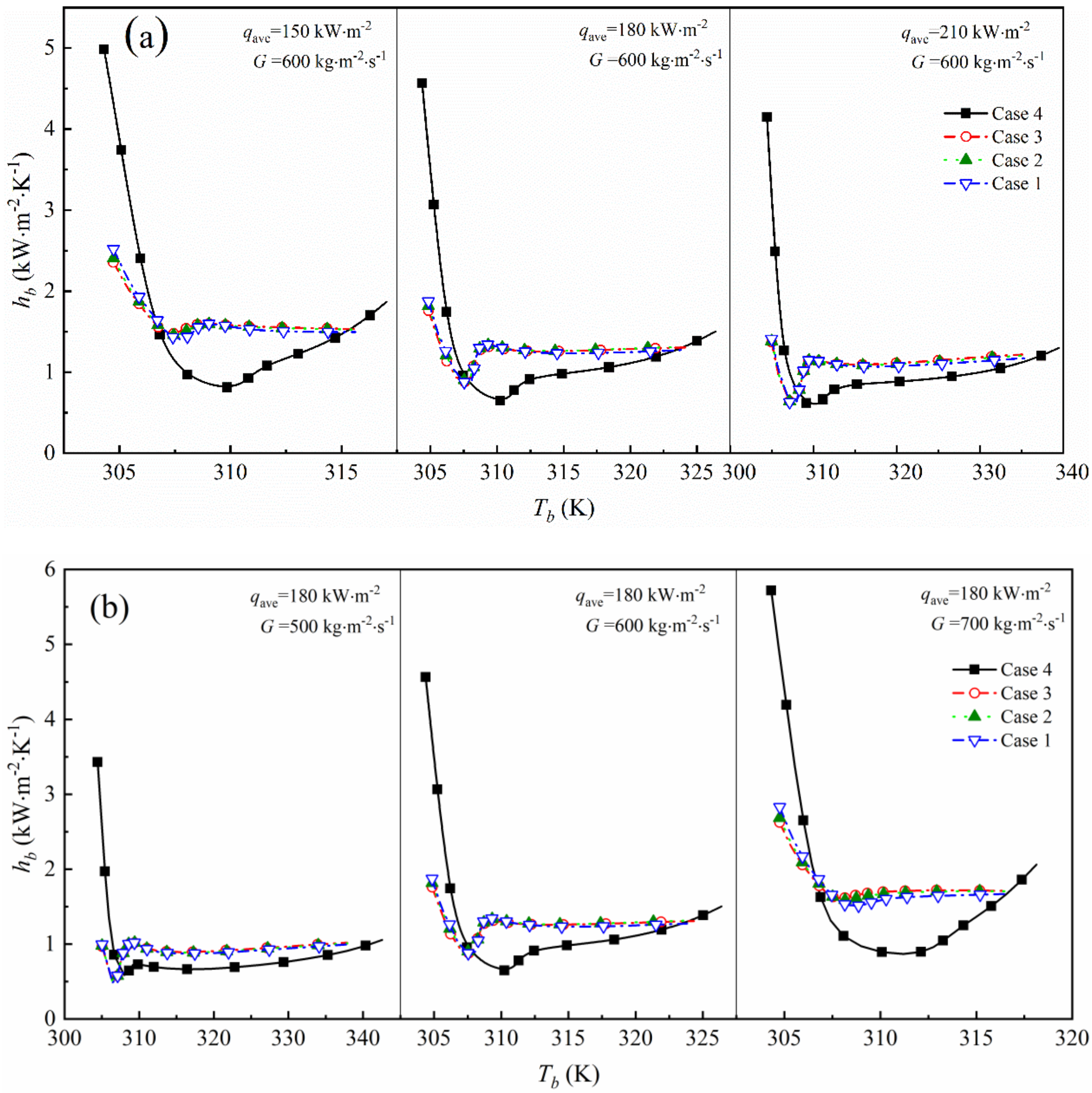

Figure 8. Local bulk heat transfer coefficient distributions under (a) various heat fluxes with mass flux of 600 kg·m^{-2}·s^{-1} and (b) various mass fluxes with heat flux of 180 kW·m^{-2} at conditions of T_{in} = 304 K, P = 8 MPa, q_{ave}= 150 to 210 kW·m^{-2} and G = 500 to 700 kg·m^{-2}·s^{-1}.

Wall temperature is an important parameter to predict the deterioration of local heat transfer. The distributions of axially outer wall (θ = 0° as shown in Figure 4) temperature T_w along the flow direction at conditions of q_{ave} = 180 kW·m^{-2} and mass flux ranging from 500 kg·m^{-2}·s^{-1} to 700 kg·m^{-2}·s^{-1} are presented in Figure. 9. When the axial heat flux is uniformly distributed, there exists a peak of T_w, where T_b are about 306.4 K and 307.3 K along the flow direction at G = 500 kg·m^{-2}·s^{-1} and G = 600 kg·m^{-2}·s^{-1}. However, the T_w increases gradually without obvious inflection point along the flow direction at G = 700 kg·m^{-2}·s^{-1}. According to the method proposed by Urbano et al. [45], if $(\mathrm{d}T_w/\mathrm{d}x)_{min} < 0$ and T_w has a significant peak under uniform heating condition, it can be considered that heat transfer deterioration has occurred. Therefore, heat transfer deterioration occurs at G = 500 kg·m^{-2}·s^{-1} and G = 600 kg·m^{-2}·s^{-1} with axially uniform heat-flux distribution, which also corresponds to the distribution of the h_b in Figure 8(b). In addition, based on the comparison between T_w and h_b distributions, it can be concluded that this criterion is still applicable to circumferentially non-uniform heating condition. For axially non-uniform heat-flux condition (Case 4), at the condition of G = 600 kg·m^{-2}·s^{-1}, the peak of T_w only appears in the place at $T_b \approx 311.0$ K, which corresponds to the minimum of h_b in Figure 8(b), and the same phenomenon is also observed at G = 700 kg·m^{-2}·s^{-1}. However, at G = 500 kg·m^{-2}·s^{-1}, two wall temperature inflection points along the flow direction can be found, one of which appears in the place at $T_b \approx 308.7$ K corresponding to the minimum value of h_b in Figure 8(b). Another inflection point is in the middle of the tube, where the heat flux is the highest. Thus, the heat transfer deterioration of SCO_2 cannot be predicted accurately only from the wall temperature inflection point under the axially non-uniform heat-flux condition.

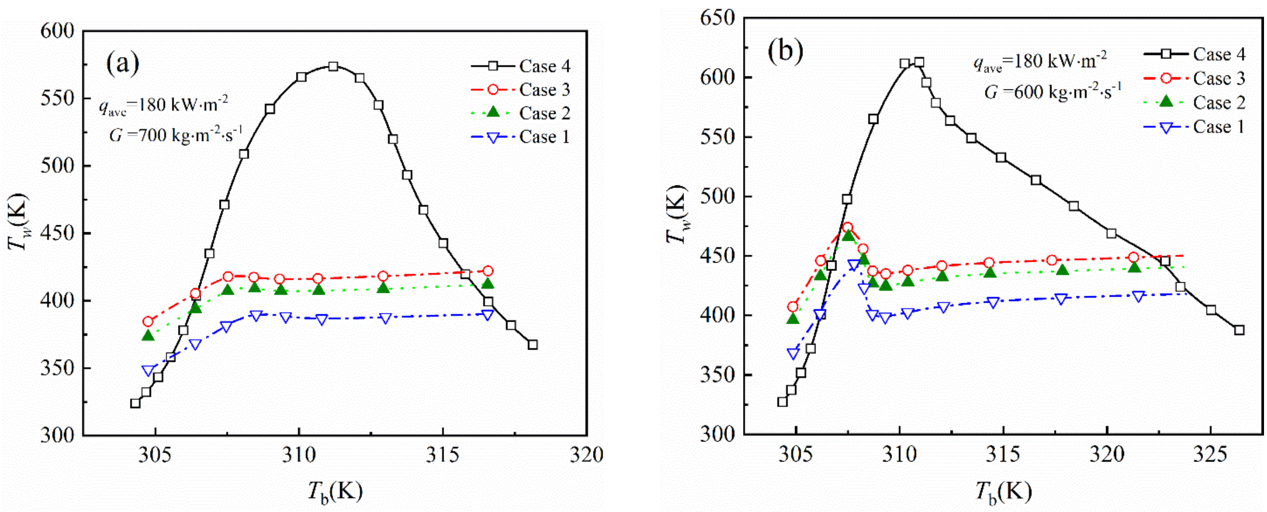

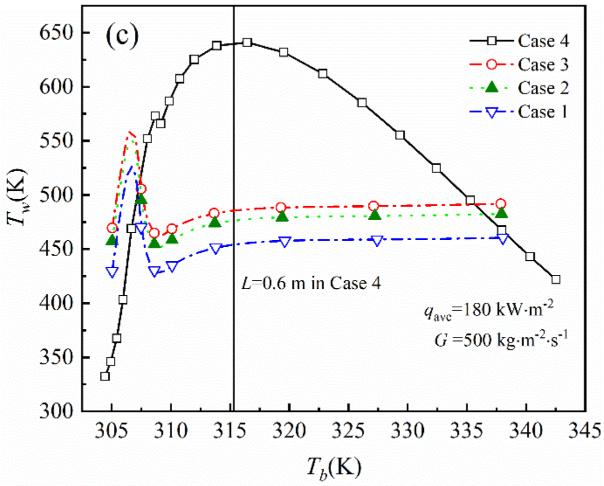

Figure 9. Axial wall temperature distributions at (a) q_{ave} = 180 kW·m^{-2} and G = 700 kg·m^{-2}·s^{-1}, (b) q_{ave} = 180 kW·m^{-2} and G = 600 kg·m^{-2}·s^{-1}, (c) q_{ave} = 180 kW·m^{-2} and G = 500 kg·m^{-2}·s^{-1} under the four types of heat-flux conditions listed in Table 1 at other conditions of T_{in} = 304 K and P = 8 MPa.

The circumferential wall-temperature distribution at the cross-section of where T_b/T_{pc} = 1 (corresponding to $z \approx 367$ mm at Case 4, $z \approx 275$ mm at Case 3, Case 2 and Case 1) under the condition of G = 600 kg·m^{-2}·s^{-1} and q_{ave} = 180 kW·m^{-2} is shown in Figure 10. The distribution of T_w is approximately similar to the distribution of heat flux. The region where the heat source is concentrated has the highest T_w in the case of unevenly circumferential heat-flux distribution. When the heat flux is uniformly distributed along the circumference, T_w is also uniformly distributed, and the local heat transfer deterioration of SCO_2 does not affect the distribution of T_w along the circumference. It can be found that T_w and circumferential wall temperature gradient at the cross-section of where T_b/T_{pc} = 1 are higher under axially non-uniform heat-flux condition than under axially uniform heating condition.

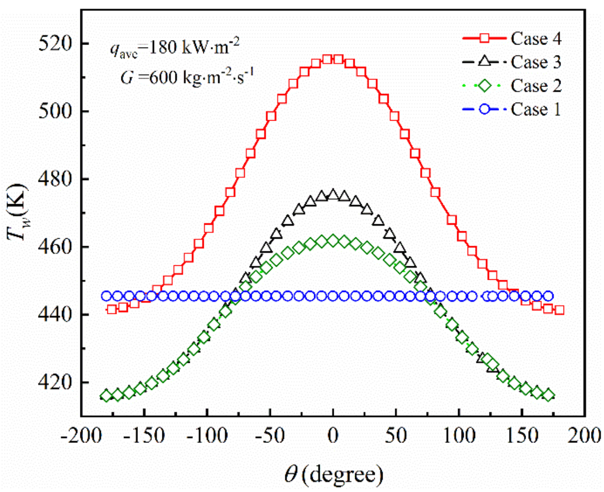

Figure 10. Circumferential wall-temperature distribution in the cross-section of where T_b/T_{pc} = 1

corresponding to $z \approx 367$ mm at Case 4, $z \approx 275$ mm at Case 3, Case 2 and Case 1 at conditions of T_{in} = 304 K, P = 8 MPa, G = 600 kg·m^{-2}·s^{-1} and q_{ave} = 180 kW·m^{-2}.

In order to further understand the differences in local heat transfer behaviours under different heat-flux conditions listed in Table 1, the wall circumferential heat transfer coefficient h_w at positions of θ = 0°and θ = 180° along the flow direction under conditions of G = 600 kg·m^{-2}·s^{-1} and q_{ave} = 180 kW·m^{-2} is demonstrated in Figure 11. The h_w follows the same trend as h_b, but h_w varies more intensely along the flow direction. When the heat flux is uniformly distributed (Case 1), the h_w is equal at locations of θ = 0°and θ = 180°. It is seen that the heat transfer is enhanced at the unheated wall (θ = 180°) under circumferentially non-uniform heat-flux conditions (Case 2 and Case 3). For axially non-uniform heating, the h_w at locations of θ = 0° and θ = 180° is almost same on the transverse section of $z \approx 0.42$ m, although the h_w of unheated wall (θ = 180°) is higher than that of heated wall (θ = 0°) on other locations along the flow direction. Since the circumferential wall temperature changes more intensely at Case 4, and the fluid temperature in the near-wall region where the heat flux is not imposed (θ = 180°) is closer to the T_{pc} than that in the heated wall (θ = 0°). Thus, the change of h_w at θ = 180° is greater than that at θ = 0° on the transverse section of $z \approx 0.42$ m.

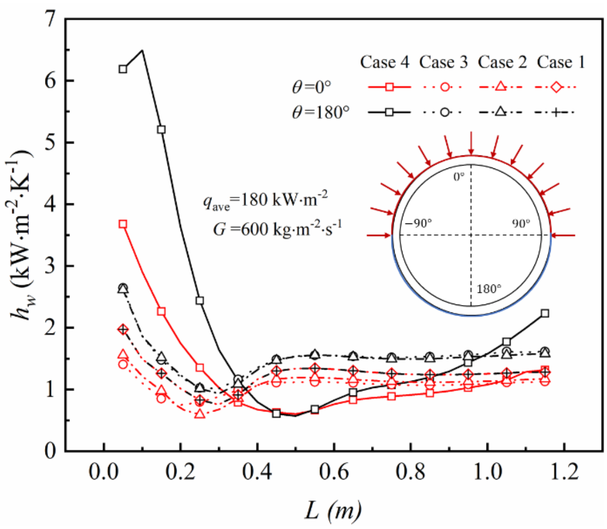

Figure 11. Distribution of local heat transfer coefficient at locations of θ = 0°and θ = 180° along the flow direction at conditions of T_{in} = 304 K, P = 8 MPa, G = 600 kg·m^{-2}·s^{-1} and q_{ave} = 180 kW·m^{-2}.

3.2. Influence of buoyancy effect

The complex heat transfer properties of SCO_2 in vertical tubes are related to buoyancy effect [46]. The buoyancy effect on the flow and heat transfer behaviours of SCO_2 in the vertical tube with different heating methods will be discussed in detail in this subsection.

To quantify the influence of buoyancy, Jackson [47] proposed a dimensionless buoyancy force factor Bo^* to determine the strength of the buoyancy force in a vertical tube. It is generally accepted that when $Bo^* > 5.6 \times 10^{-7}$, the effect of the buoyancy force cannot be ignored.

$$Bo^* = Gr^* / (Re^{3.425} Pr^{0.8}) \tag{11}$$

$$Gr^* = \frac{g\beta q d^4}{\lambda_b \nu_b^2} \tag{12}$$

$$\beta = -\frac{1}{\rho}(\frac{\partial \rho}{\partial T})_p \tag{13}$$

where β is the fluid volume expansion coefficient, Pr is Prandtl number, ν is the kinetic viscosity.

Bo^* is widely used and has been proved to have a good performance in predicting the effect of buoyancy on the heat transfer performance with vertical tubes under uniform heating condition [46, 48]. The distribution of local buoyancy factor Bo^* at conditions of G = 600 kg·m^{-2}·s^{-1} and q_{ave} = 180 kW·m^{-2} for the four types of heat-flux distributions is presented in Figure 12. The local Bo* decreases gradually along the flow direction in all cases, and the region with more significant influence on buoyancy ($Bo^* > 5.6\times10^{-7}$) is concentrated in the first half of the tube (z < 0.5 m). With the increase of T_b, the change of thermophysical properties of SCO_2 slows down and the buoyancy effect is gradually weakened. The variation trend of the Bo^* under the non-uniform heat-flux condition (Case 4, Case 3 and Case 2) is similar to that under uniform heat-flux condition (Case 1), which is in accordance with the distribution of h_b in Figure 8. Thus, Bo^* could provide a good prediction of the buoyancy effect under circumferentially and axially non-uniform heat-flux conditions. In the region where buoyancy force affects the heat transfer (z < 0.5 m), the Bo* at axially non-uniform heating condition (Case 4) is significantly greater than that at axially uniform heat-flux conditions, indicating buoyancy is more visible under axially non-uniform heating condition than under the axially uniform heating condition.

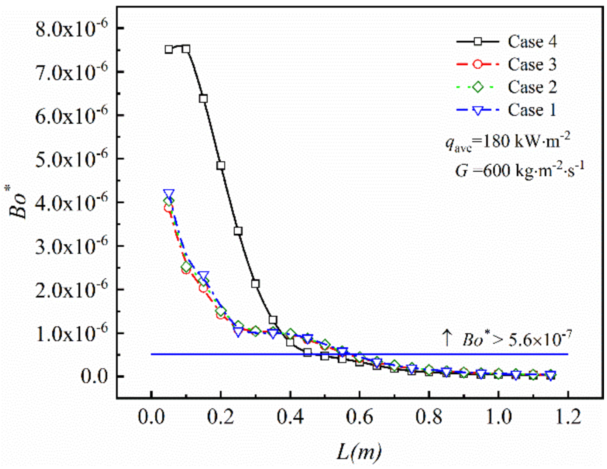

Figure 12. Distribution of local buoyancy factor Bo^* under four types of heating conditions listed in Table 1 at other conditions of T_{in} = 304 K, P = 8 MPa, G = 600 kg·m^{-2}·s^{-1} and q_{ave} = 180 kW·m^{-2}.

Three transverse sections are established (at $T_b \approx$ 305.8 K, $T_b \approx$ 307.8 K and $T_b \approx$ 317.8 K) to compare local parameters under different heat transfer performances. Heat transfer is deteriorated on the transverse section of where T_b is about 307.8 K and is restored on the cross-section of where T_b is about 317.8 K. Figure 13 shows the radial distributions of velocity v, turbulent shear stress τ and turbulent kinetic energy k on the cross-sections of where $T_b \approx$ 305.8 K (corresponding to $z \approx$ 208 mm at Case 4, $z \approx$ 120 mm at Case 3, Case 2 and Case 1), $T_b \approx$ 307.8 K (corresponding to $z \approx$ 367 mm at Case 4, $z \approx$ 275 mm at Case 3, Case 2 and Case 1), $T_b \approx$ 317.8 K (corresponding to $z \approx$ 835 mm at Case 4, $z \approx$ 955 mm at Case 3, Case 2 and Case 1) under the four types of heat-flux conditions with other conditions of G = 600 kg·m^{-2}·s^{-1} and q_{ave} = 180 kW·m^{-2}. At the cross-section of where $T_b \approx$ 305.8 K, the variation of velocity is mainly concentrated in the near-wall region, where a great velocity gradient can be observed as shown in Figure 13(a). The k is slightly suppressed at the cross-section of where $T_b \approx$ 305.8 K, and for circumferentially non-uniform heat-flux conditions (Case 3 and Case 2), it can be seen the change of k is more significant in the near-wall region with heat-flux distribution (r > 0) than that without heat-flux distribution (r < 0). When bulk temperature reaches T_{pc} ($\approx$307.8 K), a peak of velocity is formed in the near-wall region for the strong buoyancy in this region, and the velocity profile exhibits an M-shaped distribution. Non-uniform distribution of circumferential heat flux results in an asymmetric M-shaped velocity profile, which is more pronounced for axially non-uniform heating. Negative turbulent shear stress is formed because of the negative velocity gradient, and the turbulent kinetic energy is strongly suppressed at the cross-section of where $T_b \approx$ 307.8 K as shown in Figure 13(c). With the increase of the T_b, the fluid velocity increases significantly due to the decrease of density. The peak of velocity in the near-wall region disappears, and the velocity profile exhibits flat again. The turbulent kinetic energy and heat transfer capacity are restored at the cross-section of where $T_b \approx 317.8$ K.

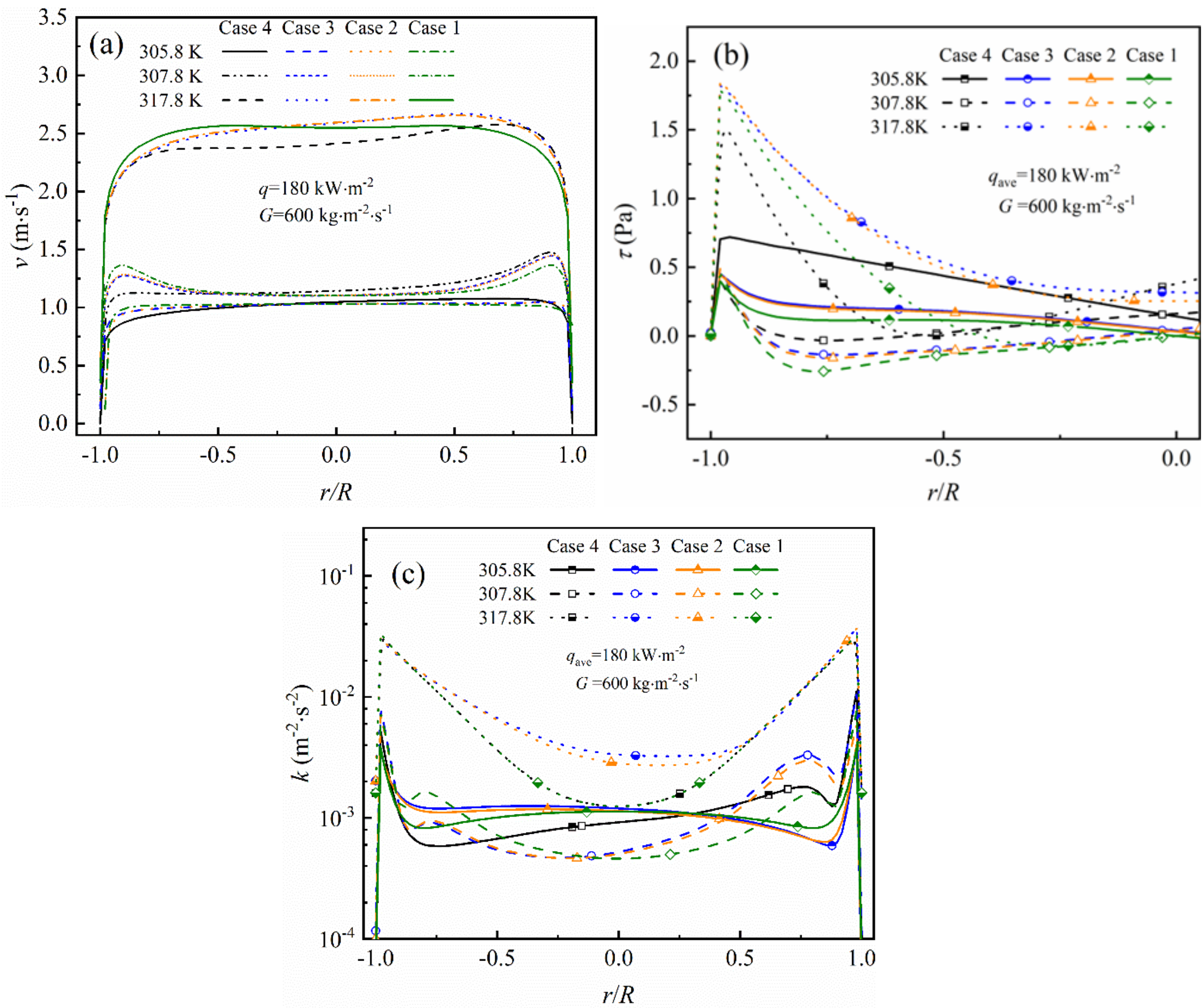

Figure 13. Radial distributions of (a) velocity, (b) turbulent shear stress and (c) turbulent kinetic energy in several cross-sections of where T_b = 305.8 K, T_b = 307.8 K and T_b = 317.8 K at conditions of T_{in} = 304 K, P = 8 MPa, G = 600 kg·m^{-2}·s^{-1}and q_{ave} = 180 kW·m^{-2}.

The turbulence production rate G_k representing the generation of turbulence kinetic energy due to mean velocity gradient can be calculated by [42]:

$$G_k = \mu_t \left(\frac{\partial u_i}{\partial x_j} + \frac{\partial u_j}{\partial x_i}\right)\frac{\partial u_i}{\partial x_j} \tag{13}$$

The distribution of turbulent production rate G_k at the cross-section of where T_b / T_{pc} = 1 (corresponding to $z \approx 367$ mm at Case 4, $z \approx 275$ mm at Case 3, Case 2 and Case 1) at the conditions of G = 600 kg·m^{-2}·s^{-1} and

q_{ave} = 180 kW·m^{-2} is illustrated in Figure 14. The buoyancy effect causes a significant reduction of G_k in the near-wall region. Under the circumferentially non-uniform heat-flux conditions (Case 3 and Case 2), the turbulent production rate in the region near the heated wall (r > 0) is smaller than that near the unheated wall (r < 0), which is not conducive to thermal diffusion. Thus, the lower wall heat transfer coefficient can be observed at the heated wall as appeared in Figure 11. For axially non-uniform heating (Case 4), the turbulent production rate presents an asymmetric distribution, and the position of the minimum G_k is not at the centre of the tube but closer to the unheated wall (r < 0), which leads to a more drastic change in the h_w on the unheated wall. Based on the above analysis, it can be seen the difference in the turbulence level of the fluid under different heating conditions plays an important role in the heat transfer performance of SCO_2.

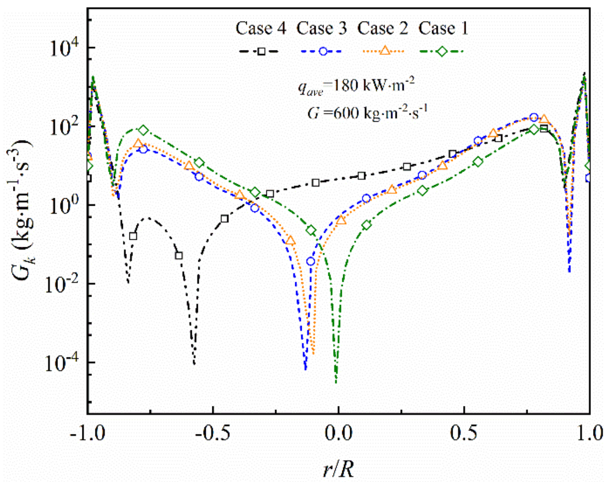

Figure 14. Radial distribution of turbulent production rate on the cross-section of where T_b/T_{pc} = 1 corresponding to $z \approx$ 367 mm at Case 4, and $z \approx$ 275 mm at Case 3, Case 2 and Case 1 respectively, at conditions of T_{in} = 304 K, P = 8 MPa, G = 600 kg·m^{-2}·s^{-1} and q_{ave} = 180 kW·m^{-2}.

The convective heat transfer of fluid is significantly affected by flow and heat transfer in the momentum and thermal boundary layer. The Prandtl number Pr could be regarded as the ratio of momentum diffusion capacity to thermal diffusion capacity, which represents the relative thickness of the momentum boundary layer and the thermal boundary layer. The turbulent boundary layer is defined by the dimensionless distance y^+ which is the ratio of the distance from the wall to viscous length scale, and the definition proposed by Bazargan et al. [49] and Hiroaki et al. [50] is employed in the present work for SCO_2, the viscous sublayer is in the region where $y^+ < 12.6$, the buffer layer is in the region where $12.6 < y^+ < 60$ and logarithmic-law layer is in the region where $60 < y^+ < 300$.

The radial distributions of fluid temperature and Pr on the cross-sections of where $T_b \approx$ 305.8 K,

$T_b \approx 307.8$ K and $T_b \approx 317.8$ K under four types of heat-flux conditions with other conditions of $q_{ave} = 180$ kW·m^{-2} and $G = 600$ kg·m^{-2}·s^{-1} are displayed in Figure 15. On the cross-section of where $T_b \approx 305.8$ K, the variation of fluid temperature is mainly concentrated in the viscous sublayer region which represents a thin thermal boundary layer. *Pr* varies dramatically in the viscous sublayer region especially under the axially non-uniform heating condition as shown in Figure 15(b). The thermal resistance is mainly concentrated in the viscous bottom layer at the cross-section of where $T_b \approx 305.8$ K. As T_b gradually approaches the T_{pc}, the change of fluid temperature is not limited to the viscous sublayer region, and the distribution of fluid temperature resembles a parabola under the axially non-uniform heat-flux condition. The thermal boundary layer becomes much thicker at this section. The value of *Pr* is larger than one, indicating the momentum boundary layer is thicker than the thermal boundary layer, and the heat transfer of SCO_2 is deteriorated at the cross-section of where $T_b \approx 307.8$ K. When the fluid bulk temperature reaches 317.8 K, the temperature profile flattens out again and the thermal boundary layer becomes thinner. The *Pr* is near one, which indicates that the momentum layer is almost as thin as the thermal layer, and the heat transfer is recovered at this cross-section. Thus, it can be obtained that the large heat transfer resistance caused by thick momentum and thermal boundary layer should be an important reason for the heat transfer deterioration.

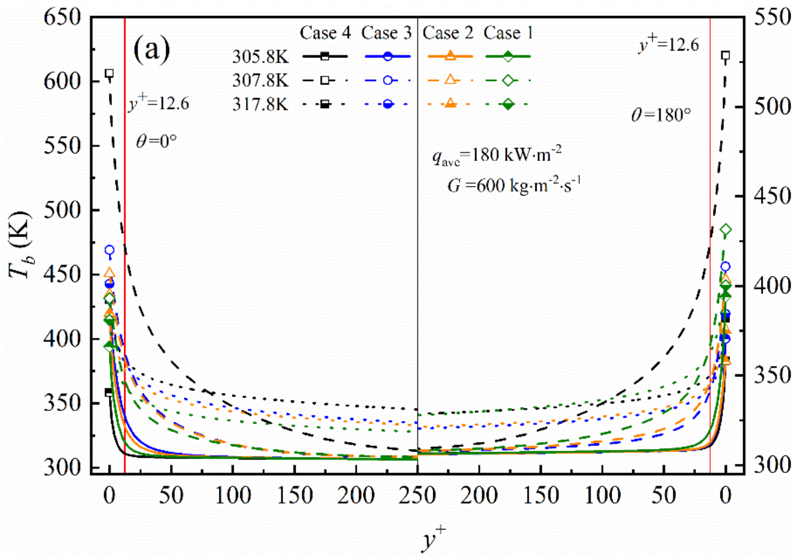

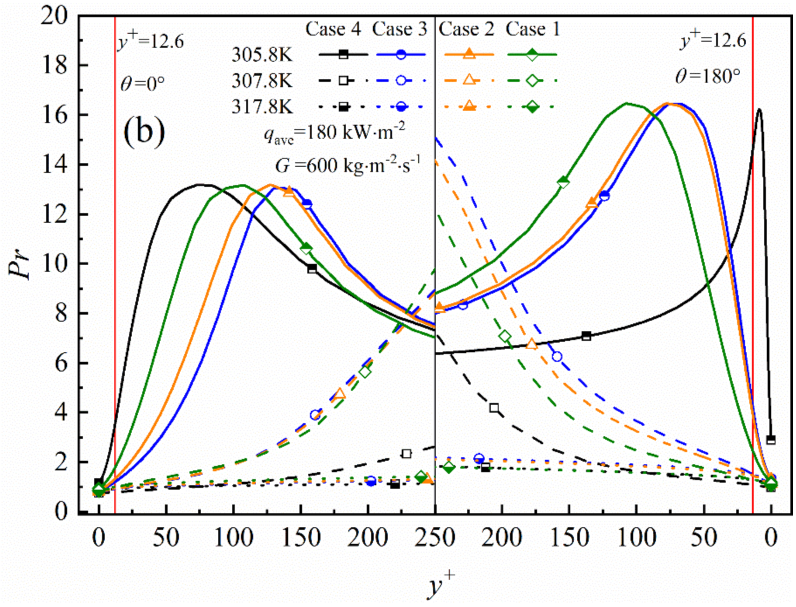

Figure 15. Radial distributions of (a) fluid temperature and (b) Prandtl number on several cross-sections of where T_b = 305.8 K, 307.8 K and 317.8 K at conditions of T_{in} = 304 K, P = 8 MPa, G = 600 kg·m^{-2}·s^{-1} and q_{ave} = 180 kW·m^{-2}.

3.3. Influence of flow direction

The effects of flow direction on heat transfer performance under non-uniform heating conditions are investigated in this subsection. Besides the vertical downward and upward flows along the *z*-axis, the thermal-hydraulic characteristics of flow without gravity is also considered as a baseline case.

The overall heat transfer coefficient *h* under the two non-uniform heating conditions of Case 4 and Case 3 for the three flows is presented in Figure 16. The vertical downward flow has the best heat transfer performance and the heat transfer performance of vertical upward flow is the worst among the three flows. The *h* of downward flow is 62.0% to 75.4% and 55.4% to 76.1% higher than that in upward flow under the axially non-uniform heat-flux condition (Case 4) and circumferentially non-uniform heat-flux condition (Case 3), respectively. The difference of *h* between downward and upward flows shrinks with the reduction of Reynolds number *Re* and the increase of heat flux. The overall heat transfer performance of Case 4 is better than that of Case 3 even in downward flow and the flow without gravity, which is the same as that of upward flow, and this discrepancy is becoming more evident with the increase of heat flux.

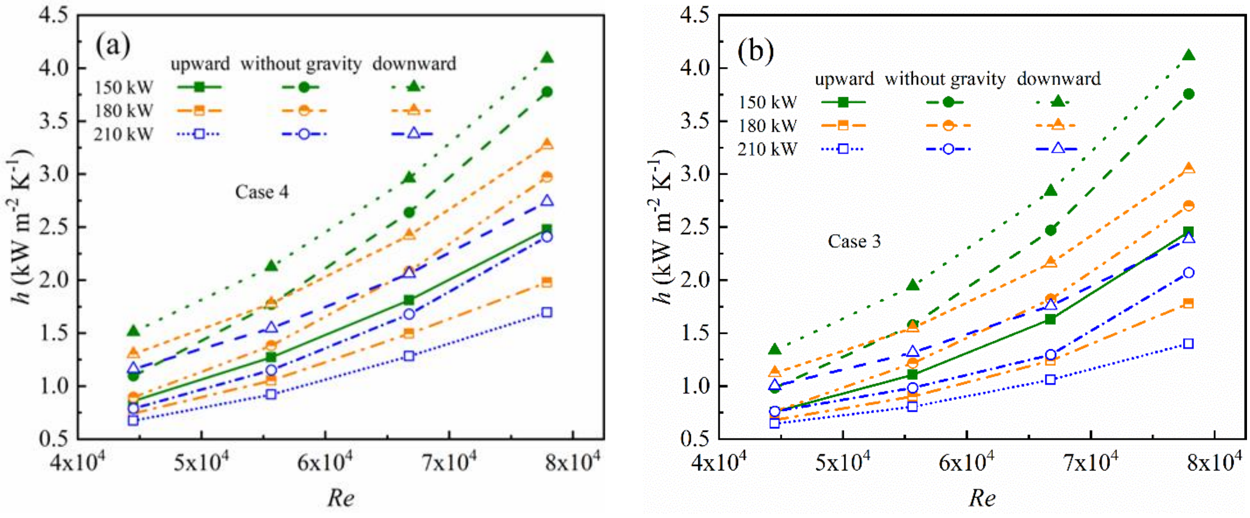

Figure 16. Overall heat transfer coefficient in Case 4 and Case 3 in upward and downward flows as well as the flow without considering gravity at conditions of T_{in} = 304 K, P = 8 MPa, q_{ave} = 150-210 kW·m^{-2} and Re = 4.4×10^{4} to 7.8×10^{4}.

Figure 17 demonstrates the temperature contours of the outer wall surface in Case 4 and Case 3 at conditions of G = 600 kg·m^{-2}·s^{-1} and q_{ave} = 180 kW·m^{-2} for the three flows, where "a" represents the vertical upward flow, "b" represents the flow without gravity and "c" represents the vertical downward flow. The wall with heat flux distribution is called as heated wall. A relatively large wall-temperature non-uniformity in the axial direction is observed in Case 4 and Case 3 especially for upward flow. Under the axially non-uniform heat-flux condition (Case 4), the maximum T_w on both heated and adiabatic wall in vertical upward flow is significantly higher than that in downward flow and the flow without gravity, and the location of maximum T_w is more forward (closer to the inlet) with upward flow. In Case 3, the maximum T_w in the vertical upward flow is obtained near the inlet of the tube, while the highest wall temperature in the vertical downward flow and the flow without gravity appears at the outlet of the tube as shown in Figure 17(b).

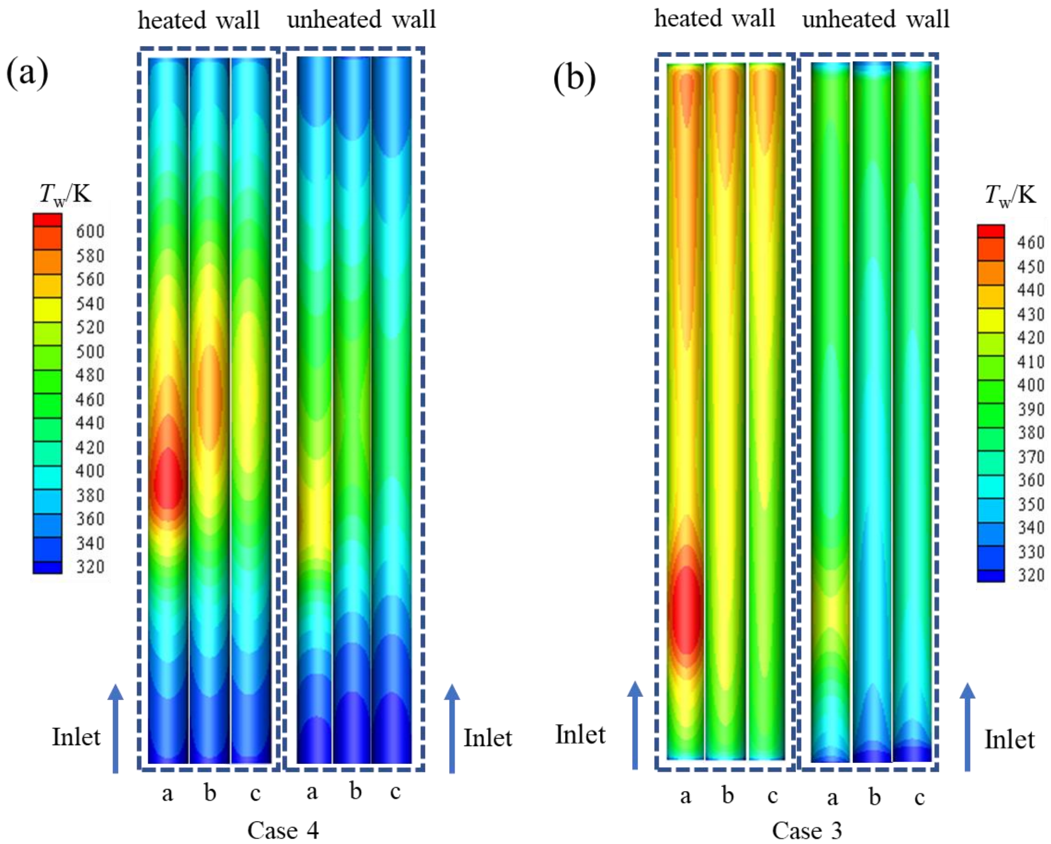

Figure 17. Contours of wall temperature of (a) Case 4 and (b) Case 3 where "a" represents the vertical upward flow, "b" represents the flow without gravity and "c" represents the vertical downward flow at conditions of T_{in} = 304 K, P = 8 MPa, G = 600 kg·m^{-2}·s^{-1} and q_{ave} = 180 kW·m^{-2}.

To further compare the local heat transfer performance in the three flows, the distributions of h_b and T_w at outer wall (θ = 0°) in Case 4 and Case 3 at conditions of G = 600 kg·m^{-2}·s^{-1} and q_{ave} = 180 kW·m^{-2} are presented in Figure 18. The h_b in downward flow and the flow without gravity is higher than that in vertical upward flow along the flow direction in Case 4 and Case 3. Under the axially uniform heat-flux condition (Case 3), both h_b and T_w vary along the flow direction without significant fluctuations in downward flow and the flow without gravity. For axially non-uniform heating (Case 4), the minimum value of h_b and the maximum value of T_w both appear in the middle of the tube where the heat flux is the largest in downward flow and the flow without gravity. It can be inferred that heat transfer deterioration does not occur where T_b is near T_{pc} in downward flow and the flow without gravity under Case 4 and Case 3. The maximum T_w in the upward flow is about 85.4 K and 22.6 K higher than that in downward flow in Case 4 and Case 3, respectively, which represents a greater axial temperature gradient in upward flow. The larger the axial temperature gradient of the wall is, the greater the thermal stress and strain become, resulting in an adverse effect on the safety and lifespan of the equipment.

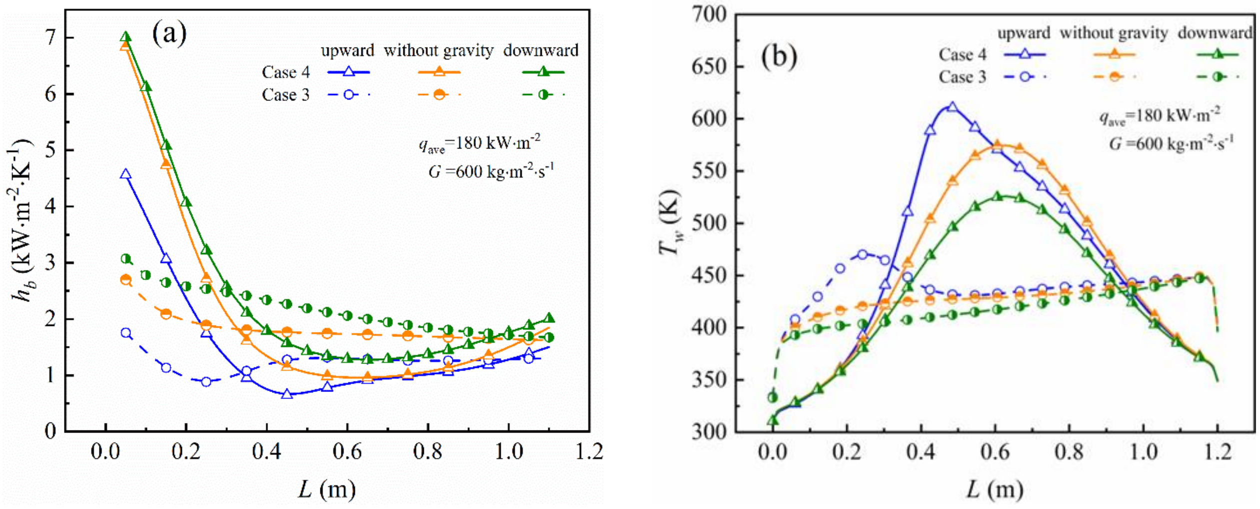

Figure 18. Distributions of (a) local heat transfer coefficient and (b) wall temperature in upward, downward flows and the flow without gravity at conditions of T_{in} = 304 K, P = 8 MPa, G = 600 kg·m^{-2}·s^{-1} and q_{ave} = 180 kW·m^{-2}.

The distributions of velocity and turbulent kinetic energy on the cross-section of where T_b/T_{pc} = 1 (corresponding to $z \approx 367$ mm in Case 4, and $z \approx 275$ mm in Case 3) under the three flows at conditions of G = 600 kg·m^{-2}·s^{-1} and q_{ave} = 180 kW·m^{-2} are shown in Figure 19. Under the condition of upward flow, the direction of buoyancy force is consistent with the flow direction and there exists a velocity peak in the near-wall region. In the downward flow, the buoyancy force is opposite to the flow direction, and it can be seen the velocity in the near-wall region is smaller than that in the flow without gravity. The turbulent kinetic energy is suppressed in the near-wall region for upward flow, which is not observed for vertical downward flow and the flow without gravity. As analysed above, the suppression of turbulent kinetic energy may be an important factor for the heat transfer deterioration.

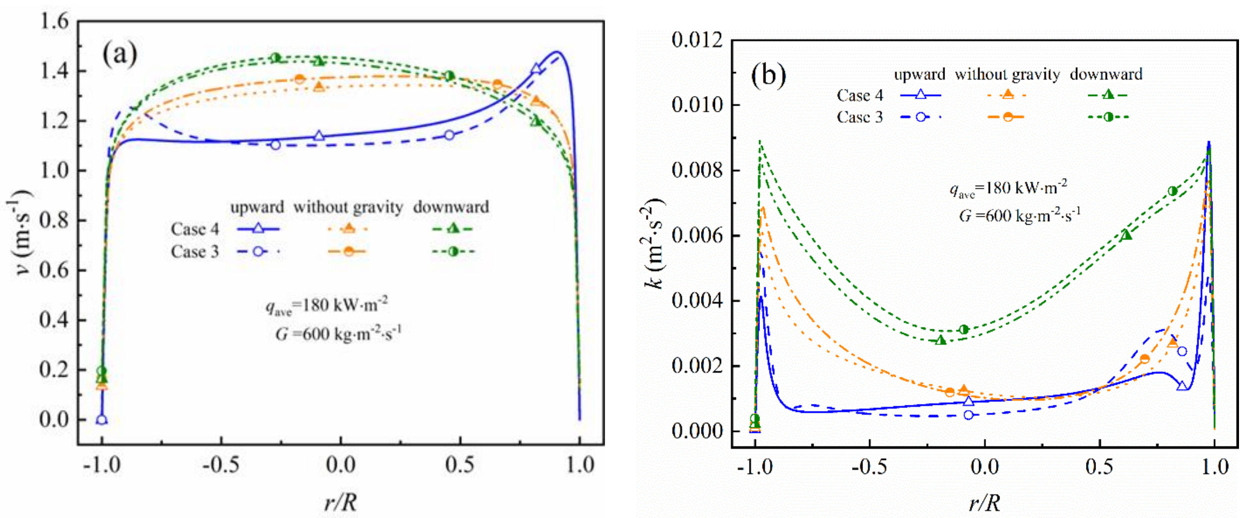

Figure 19. Radial distributions of (a) velocity, (b) turbulent kinetic energy on the cross-section of where $T_b/T_{pc} = 1$ corresponding to $z \approx 367$ mm in Case 4, $z \approx 275$ mm in Case 3 in upward and downward flows as well as the flow without considering gravity at conditions of T_{in} = 304 K, P = 8 MPa, G = 600 kg·m^{-2}·s^{-1} and q_{ave} = 180 kW·m^{-2}.

4. Conclusions

The overall and local heat transfer and flow characteristics of SCO_2 in vertical tube under the conditions of uniform heating, semi-circumferentially uniform heating, semi-circumferentially non-uniform heating and semi-circumferentially and axially non-uniform heating are numerically studied. The effects of heat flux, mass flux, and flow direction on the thermal-hydraulic characteristics of SCO_2 are investigated under conditions of q_{ave} = 150 to 210 kW·m^{-2} and G = 400 to 700 kg·m^{-2}·s^{-1}.

The overall heat transfer coefficient of axially non-uniformly heat-flux distribution is 1.2% to 20.5% higher than that of axially uniformly heat-flux distribution under conditions of q_{ave} = 150 to 210 kW·m^{-2} and $Re = 4.4 \times 10^4$ to 7.8×10^4. The overall heat transfer coefficient increased under axially non-uniform heat-flux condition, while severe local heat transfer deterioration and steep wall temperature gradient also appear, especially under high heat-flux condition. The T_b of the cross-section where heat transfer deterioration occurs in the axially non-uniformly heated tube is 1.6 K to 3.3 K higher than that of axially uniform heat flux distribution. Increasing mass flux and reducing heat flux could significantly alleviate heat transfer deterioration. The heat transfer deterioration cannot be predicted accurately only from the wall temperature inflection point under axially non-uniform heat-flux condition. Under circumferentially non-uniform heating condition, the heat transfer performance of the heated wall is better than that of the unheated wall.

The Bo^* could predict the buoyancy effect under non-uniform heat-flux conditions in the vertical tube. The buoyancy effect changes the cross-sectional velocity distribution, resulting in the difference of the turbulence of the fluid in the near-wall region under different non-uniform heat-flux conditions, which is closely related to the heat transfer performance of SCO_2. The suppression of turbulent kinetic energy and asymmetric distribution of turbulent production rate leads to severe heat transfer deterioration under axially non-uniform heating condition. The large heat transfer resistance caused by thick momentum and thermal boundary layer near the pseudocritical region should be an important reason for the heat transfer deterioration of SCO_2 under non-uniform heat-flux conditions. A thicker momentum and thermal boundary layer can be observed at the cross-section where more severe heat transfer deterioration occurs under axially non-uniform heating.

For axially and circumferentially non-uniform heating, the overall heat transfer coefficient of vertical downward flow is 62.0% to 75.4% higher than that of vertical upward flow, and this discrepancy would increase with the argument of mass flux and the reduction of heat flux. Vertical downward flow is beneficial to effectively eliminate local heat transfer deterioration and reduce axial temperature gradient, especially for axially non-uniform heat-flux condition. The present work and its conclusions could provide new knowledge of the thermohydraulic characteristics of supercritical CO_2 flows as well as practical guidance on the design and optimisation of relevant components.

Acknowledgements

This work has received funding from the CAS Project for Young Scientists in Basic Research, Grant No. YSBR-043. This work was also supported by the European Union's Horizon 2020 research and innovation programme under the Marie Skłodowska-Curie grant agreement No. [882628].

References

[1] L.F. Cabeza, A. de Gracia, A.I. Fernández, M.M. Farid, Supercritical CO_2 as heat transfer fluid: A review, Appl. Therm. Eng. 125 (2017) 799-810.

[2] A.A. Gkountas, A.M. Stamatelos, A.I. Kalfas, Recuperators investigation for high temperature supercritical carbon dioxide power generation cycles, Appl. Therm. Eng. 125 (2017) 1094-1102.

[3] F. Crespi, G. Gavagnin, D. Sánchez, G.S. Martínez, Supercritical carbon dioxide cycles for power generation: A review, Appl. Energy 195 (2017) 152-183.

[4] E.R.Casanova, C. Rubio-Maya, J.J. Pacheco-Ibarra, V.M. Ambriz-Díaz, C.E. Romero, X. Wang,

Thermodynamic analysis and optimization of supercritical carbon dioxide Brayton cycles for use with low-grade geothermal heat sources, Energy Convers. Manage. 216 (2020) 112978.

[5] M.J. Li, H.H. Zhu, J.Q. Guo, K. Wang, W.Q. Tao, The development technology and applications of supercritical CO_2 power cycle in nuclear energy, solar energy and other energy industries, Appl. Therm. Eng. 126 (2017) 255-275.

[6] K. Wang, Y.L. He, Thermodynamic analysis and optimization of a molten salt solar power tower integrated with a recompression supercritical CO_2 Brayton cycle based on integrated modeling, Energy Convers. Manage. 135 (2017) 336-350.

[7] J. Xu, E. Sun, M. Li, H. Liu, B. Zhu, Key issues and solution strategies for supercritical carbon dioxide coal fired power plant, Energy 157 (2018) 227-246.

[8] S. Dilshad, A.R. Kalair, N. Khan, Review of carbon dioxide (CO_2) based heating and cooling technologies: Past, present, and future outlook, Int. J. Energy Res. 44 (2019) 1408-1463.

[9] J. Xie, D. Liu, H. Yan, G. Xie, S.K.S. Boetcher, A review of heat transfer deterioration of supercritical carbon dioxide flowing in vertical tubes: Heat transfer behaviors, identification methods, critical heat fluxes, and heat transfer correlations, Int. J. Heat Mass Transf. 149 (2020) 119233.

[10] D.E. Kim, M.H. Kim, Experimental study of the effects of flow acceleration and buoyancy on heat transfer in a supercritical fluid flow in a circular tube, Nucl. Eng. Des. 240 (2010) 3336-3349.

[11] D.E. Kim, M.H. Kim, Experimental investigation of heat transfer in vertical upward and downward supercritical CO_2 flow in a circular tube, Int. J. Heat Fluid Flow 32 (2011) 176-191.

[12] X. Lei, J. Zhang, L. Gou, Q. Zhang, H. Li, Experimental study on convection heat transfer of supercritical CO_2 in small upward channels, Energy 176 (2019) 119-130.

[13] J.D. Jackson, W.B. Hall, Influences of buoyancy on heat transfer to fluids flowing in vertical tubes under turbulent conditions, in: S. Kakac, D.B. Spalding, Turbulent Forced Convection in Channals and Bundles, Hemisphere, New York, 1979.

[14] N. Kline, F. Feuerstein, S. Tavoularis, Onset of heat transfer deterioration in vertical pipe flows of CO_2 at supercritical pressures, Int. J. Heat Mass Transf. 118 (2018) 1056-1068.

[15] M.M. Ehsan, Z. Guan, A.Y. Klimenko, A comprehensive review on heat transfer and pressure drop characteristics and correlations with supercritical CO_2 under heating and cooling applications, Renew. Sust. Energ. Rev. 92 (2018) 658-675.

[16] J. Xie, D. Liu, H. Yan, G. Xie, S.K.S. Boetcher, A review of heat transfer deterioration of supercritical

carbon dioxide flowing in vertical tubes: Heat transfer behaviors, identification methods, critical heat fluxes, and heat transfer correlations, Int. J. Heat Mass Transf. 149 (2020) 119233.

[17] M.R. Xiang, J.F. Guo, X.L. Huai, X.Y Cui, Thermal analysis of supercritical pressure CO_2 in horizontal tubes under cooling condition, J. Supercrit. Fluids 130 (2017) 389-398.

[18] C. Li, J. Hao, X. Wang, Z. Ge, X. Du, Dual-effect evaluation of heat transfer deterioration of supercritical carbon dioxide in variable cross-section horizontal tubes under heating conditions, Int. J. Heat Mass Transf. 183 (2022) 122103.

[19] J. Wang, Z. Guan, H. Gurgenci, K. Hooman, A. Veeraragavan, X. Kang, Computational investigations of heat transfer to supercritical CO_2 in a large horizontal tube, Energy Convers. Manage. 157 (2018) 536-548.

[20] J.F. Guo, M.R. Xiang, H.Y. Zhang, X.L. Huai, K.Y. Cheng, X.Y. Cui, Thermal-hydraulic characteristics of supercritical pressure CO_2 in vertical tubes under cooling and heating conditions, Energy 170 (2019) 1067-1081.

[21] C.R. Zhao, Q.F. Liu, Z. Zhang, P.X. Jiang, H.L. Bo, Investigation of buoyancy-enhanced heat transfer of supercritical CO_2 in upward and downward tube flows, J. Supercrit. Fluids 138 (2018) 154-166.

[22] K. Wang, X. Xu, Y. Wu, C. Liu, C. Dang, Numerical investigation on heat transfer of supercritical CO_2 in heated helically coiled tubes, J. Supercrit. Fluids 99 (2015) 112-120.

[23] Y. Li, F. Sun, G. Xie, B. Sunden, J. Qin, Numerical investigation on flow and thermal performance of supercritical CO_2 in horizontal cylindrically concaved tubes, Appl. Therm. Eng. 153 (2019) 655-668.

[24] C.K. Ho, S.S. Khalsa, A Photographic Flux Mapping Method for Concentrating Solar Collectors and Receivers, J. Sol. Energy. 134 (2012) 041004.

[25] Y.L. He, K. Wang, Y. Qiu, B.C. Du, Q. Liang, S. Du, Review of the solar flux distribution in concentrated solar power: Non-uniform features, challenges, and solutions, Appl. Therm. Eng. 149 (2019) 448-474.

[26] T. Luu, D. Milani, R. McNaughton, A. Abbas, Dynamic modelling and start-up operation of a solar-assisted recompression supercritical CO_2 Brayton power cycle, Appl. Energy 199 (2017) 247-263.

[27] Y.H. Fan, G.H. Tang, X.L. Li, D.L. Yang, S.Q. Wang, Correlation evaluation on circumferentially average heat transfer for supercritical carbon dioxide in non-uniform heating vertical tubes, Energy 170 (2019) 480-496.

[28] Y.H. Fan, G.H. Tang, Numerical investigation on heat transfer of supercritical carbon dioxide in a vertical tube under circumferentially non-uniform heating, Appl. Therm. Eng. 138 (2018) 354-364.

[29] H.Y. Zhang, J.F. Guo, X.Y. Cui, X.L. Huai, Heat transfer performance of supercritical pressure CO_2 in a non-uniformly heated horizontal tube, Int. J. Heat Mass Transf. 155 (2020) 119748.

[30] H.Y. Zhang, J.F. Guo, X.Y. Cui, X.L. Huai, Performance analysis of supercritical pressure CO_2 in several enhanced tubes with non-uniform heat flux, Appl. Therm. Eng. 180 (2020) 115823.

[31] Y. Qiu, M.J. Li, Y.L. He, W.Q. Tao, Thermal performance analysis of a parabolic trough solar collector using supercritical CO_2 as heat transfer fluid under non-uniform solar flux, Appl. Therm. Eng. 115 (2017) 1255-1265.

[32] P. Schwarzbzl, R. Pitz-Paal, M. Schmitz, Visual HFLCAL - a software tool for layout and optimisation of heliostat fields, in: SolarPACES, Berlin Germany, 2009.

[33] C. He, Y. Zhao, J. Feng, An improved flux density distribution model for a flat heliostat (iHFLCAL) compared with HFLCAL, Energy. 189 (2019) 116239.

[34] K. Wang, P.S. Jia, Y. Zhang, Z.D. Zhang, T. Wang, C.H. Min, Thermal-fluid-mechanical analysis of tubular solar receiver panels using supercritical CO_2 as heat transfer fluid under non-uniform solar flux distribution, Sol. Energy 223 (2021) 72-86.

[35] Y. Liu, Y. Dong, L.T. Xie, C.Z. Zhang, C. Xu, Heat transfer enhancement of supercritical CO_2 in solar tower receiver by the field synergy principle, Appl. Therm. Eng. 212 (2022) 118479.

[36] Z. Ying, B. He, L. Su, Y. Kuang, D. He, C. Lin, Convective heat transfer of molten salt-based nanofluid in a receiver tube with non-uniform heat flux, Appl. Therm. Eng. 181 (2020) 115922.

[37] X.Z. Wang, Research on heat tranfer performance of external tubular receiver using molten salt as HTF for tower solar plant, Harbin Institute of Technology, Harbin, China, 2013.

[38] Z.J. Zheng, M.J. Li, Y.L. He, Thermal analysis of solar central receiver tube with porous inserts and non-uniform heat flux, Appl. Energy 185 (2017) 1152-1161.

[39] ANSYS CFX 16.0, solver theory guide, ANSYS Inc.2014.

[40] F.R. Menter, Two-equation eddy-viscosity turbulence models for engineering applications, AIAA Journal 32 (1994) 1598-1605.

[41] Y. Zhang, Y. Yao, Z. Li, G. Tang, Y. Wu, H. Wang, J. Lu, Low-grade heat utilization by supercritical carbon dioxide Rankine cycle: Analysis on the performance of gas heater subjected to heat flux and convective boundary conditions, Energy Convers. Manage. 162 (2018) 39-54.

[42] V.K. Garg, A.A. Ameri, Two-equation turbulence models for prediction of heat transfer on a transonic turbine blade, Int. J. Heat Fluid Flow 22 (2001) 593-602.

[43] E.W. Lemmon, M.L. Huber, M.O. Mclinden, NIST standard reference database 23: reference fluid thermodynamic and transport properties-REFPROP, version 9.0, 2007.

[44] L. Zhang, B. Zhu, X. Wu, J. Xu, Heat transfer characteristics of supercritical pressure CO_2 in a vertical smooth tube, Proceedings of the CSEE 39 (2019) 4487-4497.

[45] A. Urbano, F. Nasuti, Conditions for the occurrence of heat transfer deterioration in light hydrocarbons flows, Int. J. Heat Mass Transf. 65 (2013) 599-609.

[46] C.R. Zhao, Q.F. Liu, Z. Zhang, P.X. Jiang, H.L. Bo, Investigation of buoyancy-enhanced heat transfer of supercritical CO_2 in upward and downward tube flows, J. Supercrit. Fluids 138 (2018) 154-166.

[47] J.D. Jackson, M.A. Cotton, B.P. Axcell, Studies of mixed convection in vertical tubes, Int. J. Heat Fluid Flow 10 (1989) 2-15.

[48] X. Liu, X. Xu, C. Liu, J. Ye, H. Li, W. Bai, C. Dang, Numerical study of the effect of buoyancy force and centrifugal force on heat transfer characteristics of supercritical CO_2 in helically coiled tube at various inclination angles, Appl. Therm. Eng. 116 (2017) 500-515.

[49] M. Bazargan, M. Mohseni, The significance of the buffer zone of boundary layer on convective heat transfer to a vertical turbulent flow of a supercritical fluid, J. Supercrit. Fluids 51 (2009) 221-229.

[50] H. Tanaka, A. Tsuge, M. Hirata, N. Nishiwaki, Effects of buoyancy and of acceleration owing to thermal-expansion on forced turbulent convection in vertical circular tubes - criteria of effects, velocity and temperature profiles, and reverse transition from turbulent to laminar-flow, Int. J. Heat Mass Transf. 16 (1973) 1267-1288.